**Title**
Spectral Analysis of Vibratory Gyro Noise



**Journal**
IEEE Sensors Journal, 13(11)

**ISSN**
1530-437X

**Authors**
Kim, Dennis
M'Closkey, Robert Thomas

**Publication Date**
2013

**DOI**
10.1109/jsen.2013.2269797

Peer reviewed

# Spectral Analysis of Vibratory Gyro Noise

Dennis Kim and Robert M'Closkey, *Member, IEEE*

***Abstract*—This paper presents analysis of the noise spectra of closed-loop mode-matched vibratory gyros. Closed-form expressions for the noise-equivalent angular rate spectrum as well as the integrated angular rate (angle) variance are derived to explore the effects of modal frequency mismatch, closed-loop bandwidth, and the spectra of noise sources appearing at the sensor's input and output. It is shown that noise sources located at the output of the sensor's electromechanical transfer function create angle white noise in the closed-loop sensor. The angle white noise dominates the integrated rate behavior until it crosses the angle random walk asymptote at integration times exceeding the sensor's open-loop time constant. Even though the closed-loop sensor asymptotically recovers the angle random walk figure associated with the mode-matched open-loop sensor, the results can be used to quantify the larger integrated rate variance that is produced as a consequence of extending the sensor's bandwidth via feedback. A parameter, called the effective bandwidth, is introduced to capture the relative importance of the input noise versus output noise in determining the noise-equivalent rate spectrum. It is shown that the rate noise spectrum is robust to frequency mismatch as long as it does not exceed the effective bandwidth parameter. Empirical data obtained with a high performance MEMS vibratory gyro shows excellent agreement with the model predictions for a variety of sensor configurations including frequency-matched, frequency-mismatched, modified bandwidth, and manipulated input noise intensity cases.**

***Index Terms*—Gyroscopes, inertial navigation, microsensors, sensor phenomena and characterization, spectral analysis**

## NOMENCLATURE

$\alpha =$ coriolis coupling strength, unitless
$\Delta =$ modal frequency mismatch, rad/s
$\gamma_c =$ closed-loop scale factor, V/(deg/s)
$\gamma_0 =$ closed-loop scale factor when $\Delta = 0$, V/(deg/s)
$\gamma_{\text{OL}} =$ open-loop scale factor when $\Delta = 0$, V/(deg/s)
$\omega =$ frequency, rad/s
$\omega_\Omega =$ frequency variable associated with $\Omega$, rad/s
$\omega_c =$ closed-loop bandwidth, rad/s
$\omega_m =$ mechanical bandwidth of resonator, rad/s
$\omega_e =$ effective bandwidth, rad/s
$\omega_n =$ modal frequency of dominant sense channel mode, rad/s
$\omega_0 =$ drive mode frequency, rad/s
$\Omega_e =$ estimated angular rate, rad/s
$\nu_o =$ noise spectral density at sensor output, deg/hr/$\sqrt{\text{Hz}}$
$\nu_i =$ noise spectral density at sensor input, deg/hr/$\sqrt{\text{Hz}}$
$\Omega =$ sensor angular rate of rotation, rad/s
$\sigma_\tau^2 =$ variance of $\theta(t;\tau)$, deg$^2$
$\sigma_{\text{AV}}^2 =$ Allan variance of $\Omega_e$, (deg/hr)$^2$
$\theta(t;\tau) =$ angle change estimate over $[t-\tau, t]$ window, degree
$\tau =$ integration interval, second
$a =$ drive mode response amplitude, m
$c =$ modal damping, N/(m/s)
$d =$ rebalance signal, V
$\tilde{d} =$ scaled rebalance signal, deg/s
$H_g =$ sense channel transfer function
$j = \sqrt{-1}$
$k =$ modal stiffness, N/m
$K_f$, forcer gain of sense channel, N/V
$K_r$, rebalance gain, N/V
$K_x$, excitation channel forcer gain, N/V
$K_y =$ pick-off gain of sense channel, V/(m/s)
$m =$ modal mass of dominant sense channel mode, kg
$n_i =$ sensor input noise, V
$n_o =$ sensor output noise, V
$p =$ peak gain of sense mode, V/V
$Q =$ quality factor, unit less
$S_d =$ spectral density of $d$, V$^2$/Hz
$S_{n_i} =$ spectral density of $n_i$, V$^2$/Hz
$S_{n_o} =$ spectral density of $n_0$, V$^2$/Hz
$S_{\text{NER}} =$ spectral density of $\Omega_e$ due to noise sources, (deg/hr)$^2$/Hz
$|\cdot| =$ magnitude

This work was partially supported by DARPA contract W31P4Q-10-1-0017.

D. Kim is a Research Engineer with Mechanical and Aerospace Engineering Department, University of California, Los Angeles.

R. M'Closkey is a Professor in the Mechanical and Aerospace Engineering Department, University of California, Los Angeles, and the corresponding author.



## I. INTRODUCTION

VIBRATORY rate gyros measure the angular rate of rotation experienced by the sensor by exploiting two lightly damped Coriolis–coupled modes of a mechanical resonator when the equations of motion are written in a sensor–fixed coordinate system. High mechanical quality factors ($Q$) in vibratory rate gyros are essential to improving sensor performance with respect to various noise sources that corrupt the angular rate measurement. Although frequency-matched, or "tuned", open–loop vibratory gyros may achieve the sensor's optimum noise performance, the measurement bandwidth is limited to the resonator's intrinsic mechanical bandwidth and is practically too low for high $Q$ devices. Consequently, this paper focuses on vibratory gyros operating in a force-to-rebalance [1], or closed-loop, mode in which noise sources are present at the input and output of the electro-mechanical transfer function which represents the open-loop dynamics of the resonator that forms the heart of the sensor. In fact, expressions will be derived for the sensor transfer function and the spectrum of a single noise source located at the sensor

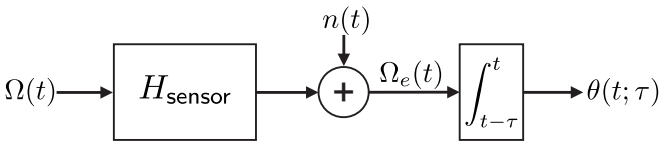


Fig. 1. Block diagram showing the relation between the sensor transfer function $H_{\text{sensor}}$, the noise equivalent rate signal $n$, and the integrated rate signal $\theta$. The input angular rate $\Omega$ is filtered by the transfer function and then corrupted by the additive noise $n$ to produce the estimated rate (denoted $\Omega_e$). The corrupted angular rate is integrated over the interval of duration $\tau$ to produce an estimate of the change in sensor orientation. The transfer function, spectral density of $n$ and the variance of $\theta$ as a function of the integration interval $\tau$ (when $\Omega(t) = 0$) are derived.

output that reflects contributions of various noise sources (see Fig. 1). Input noise sources include mechanical-thermal noise [2], sensor case vibration that couples into the modes [3], and digital-to-analog converter quantization noise. On the other hand, a common output noise source is electrical-thermal noise from analog signal conditioning [4]. In high-$Q$ sensors these noise sources conspire to produce interesting trends in the noise-equivalent rate (NER) spectrum with respect to sensor parameter perturbations. The *effective bandwidth* parameter is introduced to capture the relative importance of input noise sources versus output noise sources and it is shown that although tuned closed–loop vibratory rate gyros achieve the angle random walk (ARW) associated with tuned open–loop operation, frequency mismatch larger than the effective bandwidth raises the ARW figure for the sensor. The ARW figure is especially sensitive to output noise and when output noise is the dominant source, frequency mismatch larger than the mechanical bandwidth leads to an increase in ARW.

A closed-form expression for the mean square angle uncertainty as a function of integration time is also derived. It is shown that output noise sources create angle white noise (AWN), however, as the integration time increases, the angle variance asymptotically converges to the ARW asymptote associated with the open-loop sensor. Thus, if the physical mechanism that implements the feedback in the force-to-rebalance mode contributes negligible noise compared to the other sources, then there is no long-term noise performance penalty in operating a closed-loop sensor. Although the closed-loop and open-loop sensor (frequency-matched cases) share the same low frequency asymptote in the NER spectrum, and hence have the same ARW, there is a price to be paid for extending the sensor's bandwidth and the analysis herein precisely quantifies when, and to what degree, the closed-loop angle variance exceeds the open-loop angle variance for integration times that are longer than the open-loop time constant (this represents the interval of integration times for which open- and closed-loop variances can be compared despite the fact that these sensor configurations have very different signal bandwidths).

The motivation for this paper was prompted by the authors' testing of the Disk Resonator Gyro, or DRG [5]. The DRG provided a flexible testing platform to investigate the effects of detuning, changes in quality factor, case vibration, and buffer noise on sensor performance. Commercial signal processing boards were used in the studies in order to measure the intrinsic performance of the sensor without potential limits being introduced by more size- and energy-efficient on-chip implementations (results in Sec. VI show a low frequency noise floor less than $0.3\,\text{deg/hr}/\sqrt{\text{Hz}}$ in the frequency range extending from $0.01\,\text{Hz}$ to $0.5\,\text{Hz}$). In the course of testing the DRG it became apparent that mechanical-thermal noise, the noise source traditionally considered dominant in MEM resonators, was not the only source contributing to the NER spectrum and more thorough analysis was necessary to reveal the interplay between noise sources and resonator parameters. This paper is closest in spirit and objectives to Leland's theoretical treatment of mechanical-thermal noise in closed-loop vibratory gyros [6]. For closed-loop analysis, though, a force-to-rebalance control architecture must be assumed and we adopt a fixed gain element which is an idealization of the wide-band linear filters that have been successfully applied by the authors to the DRG and other micro-scale gyros [7], [8]. This feedback scheme, however, does not discriminate between in-phase and quadrature components of the sensing channel signal. Thus, both components are nulled and the synchronous demodulation to estimate the angular rate is performed outside of the loop which is in contrast to the force-to-rebalance loop in [6] which leaves the quadrature "channel" open. These different feedback schemes do yield differences in the NER spectrum with regard to frequency mismatch and, specifically, our approach does not see degradation in ARW when only input noise is present, which is the case considered in [6]. Our analysis approach also uses results pertaining to the spectra of modulated narrowband signals to compute the NER spectrum which departs from the slowly varying amplitude coordinates and averaging in [6]. Further comparison of force-to-rebalance architectures will not be pursued, however, some recent contributions to compact on-chip hardware implementation of vibratory gyro control and signal processing filters are given in [9], [10], [11]. Error sources, especially potential contributors to bias drift, are analyzed in [12] for several commercially available non-mode-matched MEMS gyroscopes.

The paper is organized as follows: Sec. II introduces the notation for the sensor model and the block diagram for force-to-rebalance operation; Sec. III derives the closed-loop scale factor (which is necessary in light of the assumed feedback scheme) and the expression for the closed-loop NER spectrum; Sec. IV derives an expression for the variance of the integrated rate as a function of integration time; Sec. V analyzes the noise models by considering separate cases in which the input noise is dominant, the output noise is dominant, and neither noise source is dominant; Sec. VI presents experimental results with the DRG and compares the noise model predictions to measured NER spectra and angle variance; Sec VII concludes the paper.

## II. Closed-loop Sensor Model

The fundamental model of a vibratory gyro consists of a two degree-of-freedom (DOF) resonator with Coriolis coupling terms modulated by the sensor's angular velocity. The 2-DOF

perspective is necessary when modeling such sensors since multi-channel test data is required in order to clearly identify nearly identical modal frequencies and damping that prevents the formation of classical normal modes. The sensor designer, however, goes to great lengths to decouple the two degrees of freedom so that only the Coriolis coupling terms remain. The decoupling is necessary in order to minimize the magnitude of the quadrature signal associated with the sensing pick-off which, if not minimized, can saturate the high-gain buffers. Furthermore, coupling produces offsets in the in-phase and quadrature signals which can slowly drift if the resonator dynamics are perturbed. The drift contributes to low frequency "noise" in the angular rate measurement that is independent of the noise sources considered in this paper. As in references that have preceded this work, the following idealized, time-invariant, single DOF model is useful starting point in the derivation of the NER spectrum,

$$m\ddot{y} + c\dot{y} + \alpha\Omega\dot{x} + ky = f. \tag{1}$$

In this model, $y$ represents the generalized coordinate of sense mode and $f$ represents the corresponding generalized forces that act on this degree of freedom. The degree of freedom that represents the excited mode is parameterized by the coordinate $x$. The modal mass, damping, and stiffness parameters are $m$, $c$, and $k$, respectively. The angular velocity of the resonator is denoted $\Omega$ and the Coriolis coupling strength $\alpha$ is a function of the resonator geometry. In order to provide a carrier signal onto which $\Omega$ is modulated, the vibratory rate gyro employs a feedback loop to establish a stable harmonic oscillation of $x$ (or $\dot{x}$) with oscillation frequency typically coinciding with the modal frequency of the dominant mode in this channel. Commonly implemented excitation loops include a phase–locked–loop (PLL) or feedback of the resonator velocity at the pick-off point in conjunction with automatic gain control. Both approaches are effective in maintaining a stable excitation amplitude as well as tracking shifts in the modal frequency due to changes in the resonator temperature, for example.

Open–loop vibratory rate gyros estimate $\Omega$ by demodulating the rate-induced response of $y$ (or $\dot{y}$). Closed–loop vibratory rate gyros employ a second feedback loop, commonly called the "force–to–rebalance" loop, to increase the sensor bandwidth by nulling $y$ using a feedback force through $f$ to reject the disturbance induced by the Coriolis coupling. The feedback signal is then proportional to $\alpha\Omega\dot{x}$ and an estimate of $\Omega$ is extracted by demodulating this signal with respect to $\dot{x}$. There are several force-to-rebalance filter choices whose details depend on whether the sensing pick-off measurement is proportional to $y$ or $\dot{y}$. From the perspective of control systems design, though, the optimal damping of the mode is achieved with velocity-to-force feedback so the present analysis assumes that the pick-off measures a signal proportional to $\dot{y}$. If this is not the case for a particular sensor, though, additional filters in the feedback loop must be employed to phase shift the measurement so that it in fact looks like the oscillator velocity is fed back to the forcer. This choice is optimal in the sense that the classical feedback loop sensitivity function never exceeds unity so that the feedback mechanism does not exacerbate or amplify disturbances and noise [13]. This is the objective of the rebalance loop controller irrespective of the choice of architecture (PLL, linear wide-band, and so forth). Thus, in order to focus on the closed-loop noise properties of the sensor without dwelling on the control architecture, it is assumed that a simple linear gain multiplies the measurement of $\dot{y}$ to specify the feedback signal. This configuration regulates both in-phase and quadrature components of $\dot{y}$. Readers interested in the details of the control filter design for emulating velocity-to-force feedback even in the presence of significant phase lag are directed to [8] which describes a novel gyro ASIC.

The closed–loop sense channel is shown in Fig. 2. The block $H$ represents the transfer function of the sensor dynamics from $f$ to $\dot{y}$. A complete sensor model would include details of the input and output signal conditioning dynamics, however, since they are designed to have very little gain or phase *change* in a neighborhood of sensor modes the present analysis assumes the input and output buffers to be simple noiseless elements $K_f$ and $K_y$ that converts forcer input voltage $d$ to the generalized force $f$ or, at the sensor output, converts the generalized velocity $\dot{y}$ to the buffered voltage signal $\tilde{y}$. The fixed gain $K_r$ represents the force-to-rebalance control element. The electromechanical gyro transfer function $H_g$ combines the fundamental sensor dynamics as well as the input and output gains and is given by

$$H_g(s) = \frac{K_y K_f}{m} \frac{s}{s^2 + 2\omega_m s + \omega_n^2}, \quad s \in \mathbb{C} \tag{2}$$

where $\omega_n = \sqrt{k/m}$ is the undamped natural frequency for the resonance and where the resonator's mechanical bandwidth is defined as $\omega_m := \omega_n/(2Q)$ with the modal quality factor $Q = \sqrt{mk}/c$. From the perspective of analysis, it is not necessary to individually determine the parameters $K_y$, $K_f$, and $m$ because a composite parameter representing $K_y K_f/m$ along with $\omega_n$ and $Q$ can be determined by fitting (2) to empirical frequency response data. The peak gain of (2), denoted $p$, occurs at $s = j\omega_n$, and is a useful parameter in the subsequent analysis

$$p = |H_g(j\omega_n)| = \frac{K_y K_f}{2m\omega_m}. \tag{3}$$

## III. Spectrum of angular rate noise

Two noise sources, one located at the sensor input, denoted $n_i$, and the other located at the sensor output, denoted $n_o$, are considered (see Fig. 2). The noise sources are assumed to produce stationary, zero-mean, uncorrelated signals with associated mean-square spectral densities given by $S_{n_i}$ and $S_{n_o}$. All spectral densities discussed in this paper are double-sided spectral densities and, furthermore, the mean-square analysis does not require that the noise sources posses Gaussian probability density functions but in the vast majority of cases these noise sources are Gaussian. It is natural to express the pick-off noise spectrum in terms of volts squared per hertz ($\mathrm{V}^2/\mathrm{Hz}$), however, the input noise sources are often physically located after the $K_f$ gain element because they represent forces acting on the resonator. From a measurement perspective, though, it is convenient to refer these noise sources to the input of the $K_f$ gain element and thus express them in $\mathrm{V}^2/\mathrm{Hz}$ units as well. The analysis assumes that all noise and disturbance sources are aggregated into $n_i$ and $n_o$.

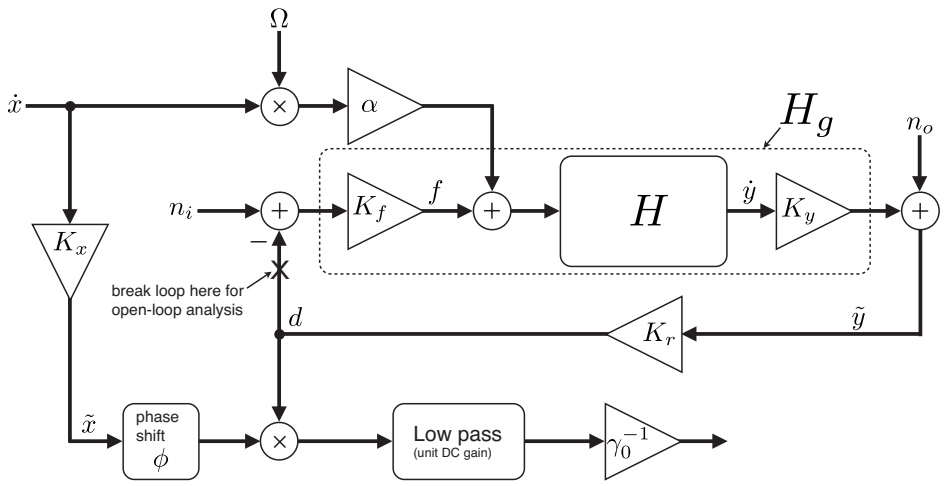


Fig. 2. Block diagram for analysis of the noise spectrum associated with the angular rate estimate, $\Omega_e$. The excitation loop is assumed to produce a stable carrier signal $\dot{x}$ by driving and tracking the companion mode. The force–to–rebalance loop shown here is designed to emulate velocity–to–force feedback so that the feedback signal $d$ regulates the noisy pick-off measurement $\tilde{y}$ to zero. The block $H$ is given by (1). The effect on $\Omega_e$ of two noise sources, denoted $n_i$ and $n_o$, are to be determined. The transfer function from $\Omega$ to $\Omega_e$ is denoted as $H_{\text{sensor}}$ in Fig. 1.

It is necessary to establish the scale factor of the sensor and the closed–loop transfer function from the rate-induced signal $(\Omega \cdot \dot{x})$ to the feedback signal $d$ is used for this purpose

$$\frac{\alpha}{K_f}\frac{K_r H_g}{1+K_r H_g} = \frac{\alpha K_r K_y}{m}\frac{s}{s^2+2\omega_c s+\omega_n^2} \tag{4}$$

where the closed–loop bandwidth $\omega_c$ is defined as

$$\omega_c = \omega_m + \frac{K_y K_f K_r}{2m} = \omega_m(1+pK_r). \tag{5}$$

It is assumed that the feedback increases the sensor bandwidth significantly beyond $\omega_m$, which requires $pK_r >> 1$ so that $\omega_c >> \omega_m$. The sensor's excitation loop regulates the $x$-DOF to a constant amplitude sinusoidal response at frequency $\omega_0$ (which may be different from the sense channel modal frequency $\omega_n$). This neglects noise that is present in the excitation loop. The input angular rate is assumed to be sinusoidal as well with amplitude $a_\Omega$ and the frequency $\omega_\Omega$

$$\begin{aligned}\dot{x}\,(t) &= -a\omega_0 \sin(\omega_0 t)\\ \Omega\,(t) &= a_\Omega \cos(\omega_\Omega t).\end{aligned}$$

The steady–state response of the control effort $d$ to the input $\Omega \cdot \dot{x}$ is

$$\begin{aligned} d\,(t) = -\frac{\alpha a a_\Omega \omega_0 K_r K_y}{2m}\Big[&\lambda \hat{D}_r(j\lambda)\cos(\lambda t)\\ &- \lambda \hat{D}_i(j\lambda)\sin(\lambda t) + \tilde{\lambda}\hat{D}_r(j\tilde{\lambda})\cos(\tilde{\lambda}t)\\ &-\tilde{\lambda}\hat{D}_i(j\tilde{\lambda})\sin(\tilde{\lambda}t)\Big]\end{aligned} \tag{6}$$

where $\lambda := \omega_0 + \omega_\Omega$, $\tilde{\lambda} := \omega_0 - \omega_\Omega$, and $\hat{D}_r\,(s)$ and $\hat{D}_i\,(s)$ are the real and imaginary parts of $\hat{D}\,(s) := 1/\left(s^2+2\omega_c s+\omega_n^2\right)$, respectively. The rate estimate $\Omega_e$ is obtained by demodulating $d$ with respect to $\tilde{x}_\phi$, where $\tilde{x}_\phi(t) := -K_x a\omega_0 \sin(\omega_0 t+\phi)$ is a phase-shifted copy of the measurement of $\dot{x}$, and normalizing by the closed-loop scale factor $\gamma_c$,

$$\begin{aligned}\Omega_e(t) &= \mathcal{LP}\left[\frac{1}{\gamma_c}\tilde{x}_\phi(t)d(t)\right]\\ &= \frac{K_x a\omega_0}{\gamma_c}\mathcal{LP}\left[-\sin(\omega_0 t+\phi)d(t)\right].\end{aligned} \tag{7}$$

The "$\mathcal{LP}[\cdot]$" operator denotes unity DC gain low pass filtering of its argument with bandwidth $\omega_{lp}$. The scale factor is determined when a constant angular rotation rate is applied, in other words if $\omega_\Omega = 0$ then the following constant is produced for the angular rate,

$$\Omega_e(t) = \frac{1}{\gamma_c}\frac{\alpha a^2\omega_0^3}{2m}K_r K_x K_y \left|\hat{D}\,(j\omega_0)\right| a_\Omega \sin\left(\phi - \angle\hat{D}\,(j\omega_0)\right) \tag{8}$$

where $|\hat{D}\,(j\omega_0)\,|$ and $\angle\hat{D}\,(j\omega_0)$ are the magnitude and phase of $\hat{D}\,(j\omega_0)$. The optimal demodulation phase, given by $\phi_d := \pi/2 + \angle\hat{D}\,(j\omega_0)$, maximizes (8) and rejects any components that are in quadrature with the rate-induced signal. Note $\angle\hat{D}(j\omega_0) \approx -\pi/2$ radians when $\omega_0$ is in a neighborhood of $\omega_n$ so $\phi_d \approx 0$ radians. The optimal demodulation phase can deviate significantly from this value if the pick-off signal conditioning contributes phase lag to the measurements of $\dot{x}$ and $\dot{y}$, however, these effects are not included in the present analysis. The closed-loop scale factor is defined so that $\Omega_e = a_\Omega$ when $\phi = \phi_d$,

$$\begin{aligned}1/\gamma_c &= \frac{4m}{\alpha a^2\omega_0^2 K_x K_y K_r}\sqrt{\left(\frac{\omega_n^2-\omega_0^2}{2\omega_0}\right)^2+\omega_c^2}\\ &= \frac{2K_f}{\alpha a^2\omega_0^2 K_x}\frac{1+pK_r}{pK_r}\sqrt{1+\left(\frac{\omega_n^2-\omega_0^2}{2\omega_c\omega_0}\right)^2}.\end{aligned} \tag{9}$$

The *detuning* frequency is defined as $\Delta := \omega_0 - \omega_n$ and quantifies the difference between the resonant frequency of the sensing channel and the operating frequency of the drive

channel. Since $(\omega_n^2 - \omega_0^2)/(2\omega_c\omega_0)$ is well-approximated by $-\Delta/\omega_c$, (9) shows that the closed-loop scale factor is insensitive to detuning so long as the detuning is small compared to the closed-loop bandwidth. Furthermore, it is also evident that $\gamma_c$ is insensitive to changes in the rebalance gain $K_r$ and to changes in the quality factor so long as the maximum loop gain magnitude satisfies $pK_r >> 1$. Additional details given in [7] shows that optimal demodulation phase $\theta_d$ also shares these insensitivities to $\Delta$, quality factor and rebalance gain under the same assumptions. The *nominal* scale factor, denoted $\gamma_0$, is obtained when $\Delta = 0$,

$$1/\gamma_0 = \frac{2K_f}{\alpha a^2 \omega_0^2 K_x} \frac{1 + pK_r}{pK_r}. \tag{10}$$

The nominal scale factor will be used in the subsequent analysis.

The sensor transfer function can be derived from (7) as well. Only the case $\omega_0 = \omega_n$, that is, $\Delta = 0$, is considered since the calculations are lengthy and tedious when $\Delta \neq 0$. When $\Delta = 0$, (7) reduces to

$$\begin{aligned}\Omega_e(t) = -a_\Omega \omega_c \Bigg( & \Big(\omega_n(\hat{D}_r(j\lambda) - \hat{D}_r(j\tilde{\lambda})) \\ & + \omega_\Omega(\hat{D}_r(j\lambda) + \hat{D}_r(j\tilde{\lambda}))\Big) \sin\omega_\Omega t \\ & + \Big(\omega_n(\hat{D}_i(j\lambda) + \hat{D}_i(j\tilde{\lambda})) \\ & + \omega_\Omega(\hat{D}_i(j\lambda) - \hat{D}_i(j\tilde{\lambda}))\Big) \cos\omega_\Omega t \Bigg),\end{aligned} \tag{11}$$

where the low pass operation has been used to discard components with frequencies in a neighborhood of $2\omega_n$. Further simplification is possible when $|\omega_\Omega| << \omega_n$. This is a reasonable assumption since the resonant frequency of the oscillator is intended to act as high frequency carrier onto which the angular rate signal is modulated. With this assumption

$$\begin{aligned}\hat{D}(j\lambda) &\approx \frac{1}{-2\omega_n\omega_\Omega + j2\omega_c\omega_n}, \\ \hat{D}(j\tilde{\lambda}) &\approx \frac{1}{2\omega_n\omega_\Omega + j2\omega_c\omega_n}\end{aligned}$$

and (11) reduces to

$$\begin{aligned}\Omega_e(t) &= -a_\Omega\omega_c\left(2\omega_n\hat{D}_r(j\lambda)\sin\omega_\Omega t + 2\omega_n\hat{D}_i(j\lambda)\cos\omega_\Omega t\right) \\ &= a_\Omega\omega_c\left(\frac{\omega_\Omega}{\omega_\Omega^2 + \omega_c^2}\sin\omega_\Omega t + \frac{\omega_c}{\omega_\Omega^2 + \omega_c^2}\cos\omega_\Omega t\right) \\ &= a_\Omega \frac{1}{\sqrt{(\omega_\Omega/\omega_c)^2 + 1}} \cos\left(\omega_\Omega t - \tan^{-1}(\omega_\Omega/\omega_c)\right)\end{aligned}$$

Since $\Omega(t) = a_\Omega \cos\omega_\Omega t$, the transfer function from $\Omega$ to $\Omega_e$ in Fig. 2 is

$$H_{\text{sensor}} = \frac{1}{s/\omega_c + 1}. \tag{12}$$

This transfer function is also inserted into the block diagram in Fig. 1. Although not derived here, $H_{\text{sensor}}$ is insensitive to $\Delta$ so long as $|\Delta| << \omega_c$.

In order to complete the description of the signals in Fig. 1 the interpretation of $d$ is now changed from a signal induced by angular motion of the sensor to a stochastic signal due to noise sources $n_o$ and $n_i$ shown in Fig. 2. The analysis in [6] essentially considers the same model (with $n_o = 0$) expressed in a slowly varying amplitude coordinates system. Our analysis approach determines the NER spectrum as the spectrum of a modulated random process. This perspective gives quite a bit of insight into the role of the noise sources, effects of detuning and so forth. The spectral density of $d$ due solely to the noise sources is

$$S_d(\omega) = \left|\frac{K_r}{1 + K_r H_g(j\omega)}\right|^2 \left(S_{n_o} + |H_g(j\omega)|^2 S_{n_i}\right) \tag{13}$$

where $S_d$ is expressed in $\text{V}^2/\text{Hz}$. The signal $\tilde{d}$ is defined as $\tilde{d} := (K_x a\omega_0/\gamma_0)d$, in other words, $d$ scaled by the amplitude of $\dot{x}$ and divided by $\gamma_0$. This yields a signal whose units are those of angular rate. The spectral density of $\tilde{d}$ is

$$\begin{aligned}S_{\tilde{d}}(\omega) &= \left(\frac{K_x a\omega_0}{\gamma_0}\right)^2 S_d(\omega) \\ &= \left|\frac{K_r}{1 + K_r H_g(j\omega)}\right|^2 \Bigg(\left(\frac{K_x a\omega_0}{\gamma_0}\right)^2 S_{n_o} \\ &\qquad + |H_g(j\omega)|^2 \left(\frac{K_x a\omega_0}{\gamma_0}\right)^2 S_{n_i}\Bigg).\end{aligned}$$

At this point some simplifying, though reasonable, assumptions are made. It is assumed that the densities $S_{n_o}$ and $S_{n_i}$ are constant in a neighborhood of $\omega_0$ that encompasses the closed-loop bandwidth so that the scaled densities can be assigned the constants $\nu_o, \nu_i > 0$,

$$\nu_o^2 := (K_x a\omega_0/\gamma_0)^2 S_{n_o}, \quad \nu_i^2 := (K_x a\omega_0/\gamma_0)^2 S_{n_i}, \tag{14}$$

and, thus, after some manipulation, $S_{\tilde{d}}$ can be written

$$S_{\tilde{d}}(\omega) = K_r^2\nu_o^2 \frac{(\omega_n^2 - \omega^2)^2 + (2\omega_e\omega)^2}{(\omega_n^2 - \omega^2)^2 + (2\omega_c\omega)^2}, \tag{15}$$

where the parameter $\omega_e$ is the *effective bandwidth*

$$\omega_e = \omega_m\sqrt{1 + \left(\frac{p\nu_i}{\nu_o}\right)^2}. \tag{16}$$

The effective bandwidth describes the effect of the relative power in $d$ due to the noise sources at the sensor's input and output and is especially useful in determining if detuning increases the noise equivalent rate spectrum –more details are provided in Sec. V. As the output noise becomes less significant ($\nu_o \to 0$ for fixed $\nu_i$), then $\omega_e \to \infty$. Conversely, if $\nu_i \to 0$ for fixed $\nu_o$, then $\omega_e \to \omega_m$.

The NER spectral density is obtained by demodulating $S_{\tilde{d}}$ with respect to $\sin(\omega_0 t + \phi)$ (the phase $\phi$ has no impact on the resulting spectrum). In practice, the bandwidth of the rebalance controller filter limits the support of $S_{\tilde{d}}$ and, furthermore, the low-pass filtering operation after demodulation by $\dot{x}$ is equivalent to bandpass filtering $d$ with passband $2\omega_{lp}$ centered at $\omega_0$ prior to demodulation by $\dot{x}$. The demodulation frequency $\omega_0$, however, is typically several orders of magnitude larger than the filter bandwidth, that is $\omega_0 >> \omega_{lp}$, thus, the bandpass filtered noise is a narrowband process and the NER spectral density (denoted $S_{\text{NER}}$) assumes a simple form [14],

$$S_{\text{NER}}(\omega) = \frac{1}{4}\left(S_{\tilde{d}}(\omega_0 + \omega) + S_{\tilde{d}}(\omega_0 - \omega)\right), \tag{17}$$

where $\omega$ is constrained to the interval $[-\omega_{lp}, \omega_{lp}]$ and $S_{\tilde{d}}$ is given by (15). Although the exact expression for $S_{\text{NER}}$ is lengthy the following is derived

$$S_{\text{NER}}(\omega) = \frac{1}{2}\left(\frac{K_r}{\omega_c}\right)^2 \nu_o^2 \left(\Delta^2 + \omega_c^2\right) \cdot \frac{\left(\Delta^2 + \omega_c^2 + \omega^2\right)\left(\Delta^2 + \omega_e^2 + \omega^2\right) - (2\Delta\omega)^2}{\left((\Delta-\omega)^2 + \omega_c^2\right)\left((\Delta+\omega)^2 + \omega_c^2\right)}, \tag{18}$$

under the following assumptions

1) the noise sources can be treated as narrowband processes, i.e. $\omega_{lp} << \omega_0$,
2) the closed-loop bandwidth is more than an order of magnitude smaller than the demodulation frequency, i.e. $\omega_c << \omega_0$,
3) the modal frequency detuning is an order of magnitude smaller than the closed-loop bandwidth, i.e. $\Delta << \omega_c$.

This expression is taken to be the noise-equivalent rate spectral density in remainder of the paper.

## IV. Angle uncertainty

### A. Integrated rate uncertainty

Integrating $\Omega_e$ over a $\tau$ second window gives an estimate of the change in orientation experienced by the sensor over that interval with respect to an inertial reference frame. In other words

$$\theta(t;\tau) = \int_{t-\tau}^{t} \Omega_e(t)dt. \tag{19}$$

where $\theta(t;\tau)$ denotes the change in orientation at time $t$ obtained by integrating the angular rate estimate over the preceding $\tau$ seconds. The noise associated with the angular rate estimate contributes to uncertainty in the derived orientation change. The impulse response of the integration operation is

$$h_\tau(t) = \begin{cases} 1 & t \in [0,\tau] \\ 0 & t \notin [0,\tau] \end{cases}. \tag{20}$$

The Fourier transform of $h_\tau$ is

$$H_\tau(\omega) = \frac{1}{j\omega}\left(1 - e^{-j\tau\omega}\right).$$

For fixed $\tau$, the mean square value of $\theta(t;\tau)$ due to the rate noise with spectral density $S_{\text{NER}}$ is denoted $\sigma_\tau^2$ and can be computed from

$$\begin{aligned}\sigma_\tau^2 :&= \frac{1}{2\pi}\int_{-\infty}^{\infty} S_{\text{NER}}(\omega)|H_\tau(\omega)|^2 d\omega \\ &= \frac{1}{2\pi}\int_{-\infty}^{\infty} S_{\text{NER}}(\omega)\left|\frac{1}{j\omega}\left(1 - e^{-j\tau\omega}\right)\right|^2 d\omega.\end{aligned} \tag{21}$$

Substituting (18) into (21) yields,

$$\sigma_\tau^2 = \frac{1}{4\pi}\left(\frac{K_r\nu_o}{\omega_c}\right)^2 \left(\Delta^2 + \omega_c^2\right) I, \tag{22}$$

where

$$I = \int_{-\infty}^{\infty} \frac{\left(\Delta^2 + \omega_c^2 + \omega^2\right)\left(\Delta^2 + \omega_e^2 + \omega^2\right) - (2\Delta\omega)^2}{\left((\Delta-\omega)^2 + \omega_c^2\right)\left((\Delta+\omega)^2 + \omega_c^2\right)} \cdot \left|\frac{1}{j\omega}\left(1 - e^{-j\tau\omega}\right)\right|^2 d\omega. \tag{23}$$

Contour integration is used to evaluate (23) (see the Appendix for details) and produces the following expression for the mean square value of the angle uncertainty as a function of the integration interval

$$\begin{aligned}\sigma_\tau^2 = \frac{1}{2}\left(\frac{K_r}{\omega_c}\right)^2 \nu_o^2 \Bigg[&\left(\Delta^2 + \omega_e^2\right)\tau \\ &+ \frac{\omega_c^2 - \omega_e^2}{\omega_c(\Delta^2 + \omega_c^2)}\Big(\left(\omega_c^2 - \Delta^2\right)\left(1 - \cos(\Delta\tau)e^{-\omega_c\tau}\right) \\ &+ 2\Delta\omega_c \sin(\Delta\tau)e^{-\omega_c\tau}\Big)\Bigg].\end{aligned} \tag{24}$$

The DC value of $S_{\text{NER}}$ is

$$S_{\text{NER}}(0) = \frac{1}{2}\left(\frac{K_r}{\omega_c}\right)^2 \nu_o^2 \left(\Delta^2 + \omega_e^2\right)$$

so $\sigma_\tau^2$ can be written

$$\sigma_\tau^2 = S_{\text{NER}}(0)\tau + \text{terms bounded in } \tau.$$

Thus, the angle random walk (ARW) associated with the sensor is determined by $S_{\text{NER}}(0)$, however, the terms bounded in $\tau$ contribute interesting trends to $\sigma_\tau$ that will be discussed in Section V.

### B. Allan variance representation

The Allan variance [15], denoted $\sigma_{\text{AV}}^2(\tau)$, can be computed from the rate noise power spectrum according to

$$\sigma_{\text{AV}}^2(\tau) = \frac{1}{\pi}\int_{-\infty}^{\infty} S_{\text{NER}}(\omega)\frac{\sin^4\left(\frac{1}{2}\omega\tau\right)}{\left(\frac{1}{2}\omega\tau\right)^2}d\omega.$$

This expression can be rewritten as

$$\sigma_{\text{AV}}^2(\tau) = \frac{1}{4\pi}\int_{-\infty}^{\infty} S_{\text{NER}}(\omega)\frac{1}{(\tau\omega)^2}\left|1 - e^{-j\tau\omega}\right|^4 d\omega, \tag{25}$$

and the similarities with (21) are evident. The $1/\tau^2$ factor in (25) coverts the "moving" integration operation into a moving average. Furthermore, the additional $|1 - e^{-j\tau\omega}|^2$ factor in (25) derives from the differencing operation between the current and $\tau$-delayed signals. The same contour for evaluating (21) is used to compute (25) and this yields the closed-form Allan variance expression

$$\begin{aligned}\sigma_{\text{AV}}^2(\tau) = S_{\text{NER}}(0)\frac{1}{\tau} + \frac{1}{\tau^2}\beta\Bigg[&\left(\omega_c^2 - \Delta^2\right)\left(\frac{3}{2} - 2e^{-\tau\omega}\cos\tau\Delta\right. \\ &\left. + \frac{1}{2}e^{-2\tau\omega_c}\cos 2\tau\Delta\right) + 2\omega_c\Delta\left(2e^{-\tau\omega_c}\sin\tau\Delta\right. \\ &\left. - \frac{1}{2}e^{-2\tau\omega_c}\sin 2\tau\Delta\right)\Bigg],\end{aligned} \tag{26}$$

where $\beta$ is the constant

$$\beta = \frac{1}{2}\left(\frac{K_r}{\omega_c}\right)^2 \nu_o^2 \frac{\omega_c^2 - \omega_e^2}{\omega_c(\omega_c^2 + \Delta^2)}.$$

## V. Discussion

The expression for $S_{\text{NER}}$ is a complicated function of $\Delta$, $\omega_e$ and $\omega_c$ but its features can be studied by considering $S_{\text{NER}}(\omega)$ when $\Delta = 0$, and the value of $S_{\text{NER}}(0)$ when $\Delta \neq 0$. Although the sensor's ARW is determined by $S_{\text{NER}}(0)$, there are other trends in $S_{\text{NER}}$ that impact $\sigma_\tau$ which need to be elucidated. Furthermore, it will be demonstrated that depending on the relative importance of the noise sources, $S_{\text{NER}}(0)$ may be more or less susceptible to detuning, changes in quality factor and so forth. Three closed-loop scenarios are studied: *Input noise dominates* addresses the situation when the output noise can be neglected ($\omega_e \to \infty$ as $\nu_o \to 0$); *No dominant noise source* addresses the situation when both input and output noise sources are important in determining properties of the noise equivalent rate spectrum; *Output noise dominates* addresses the situation when $\omega_e = \omega_m$ because $\nu_i = 0$, that is, the input noise can be ignored. This section also discusses the response of $S_{\text{NER}}$ to changes in the resonance quality factor and a brief comparison between the tuned open- and closed-loop NER spectra is made as well.

### A. $S_{NER}(\omega)$ when $\Delta = 0$

First consider $S_{\text{NER}}$ under the assumption $\Delta = 0$, in other words, the sense mode frequency $\omega_n$ and excitation loop operating frequency $\omega_0$ are equal,

$$S_{\text{NER}}(\omega) = \frac{1}{2} K_r^2 \nu_o^2 \frac{\omega^2 + \omega_e^2}{\omega^2 + \omega_c^2}. \tag{27}$$

*Input noise dominates.* Since $(\nu_o \omega_e)^2 = \omega_m^2(\nu_o^2 + (p\nu_i)^2) \to (\omega_m p \nu_i)^2$, as $\nu_o \to 0$, (27) reduces to

$$S_{\text{NER}}(\omega) = \frac{1}{2} \nu_i^2 \frac{\omega_c^2}{\omega^2 + \omega_c^2}. \tag{28}$$

The NER spectrum when input noise is dominant has a low-pass characteristic that rolls off at frequencies outside of the band $[-\omega_c, \omega_c]$. The pass band value of $S_{\text{NER}}$ is approximately $\nu_i^2/2$. An example of $S_{\text{NER}}^{\frac{1}{2}}$ in this case is shown in Fig. 3.

*No dominant noise source*. There is no simplification of (27). The high frequency asymptote of $S_{\text{NER}}$ is

$$\lim_{|\omega| \to \infty} S_{\text{NER}} = \frac{1}{2}(K_r \nu_o)^2 \tag{29}$$

which does not depend on the input noise and is seen to be proportional to the square of the force-to-rebalance feedback gain and output noise. The value of $S_{\text{NER}}$ at $\omega = 0$ reduces to

$$S_{\text{NER}}(0) = \frac{1}{2}\left(\left(\frac{\nu_o}{p}\right)^2 + \nu_i^2\right), \tag{30}$$

however, if $\omega_e > \omega_c$ then the input noise essentially dictates $S_{\text{NER}}$ because (27) has the shape of a lag filter that closely approximates (28) when $\omega \in [-\omega_0, \omega_0]$ and $S_{\text{NER}}(0) \approx \nu_i^2/2$. On the other hand, when $\omega_e < \omega_c$, (27) has a lead filter shape –see Fig. 3. The role of the effective bandwidth $\omega_e$ is evident in this figure.

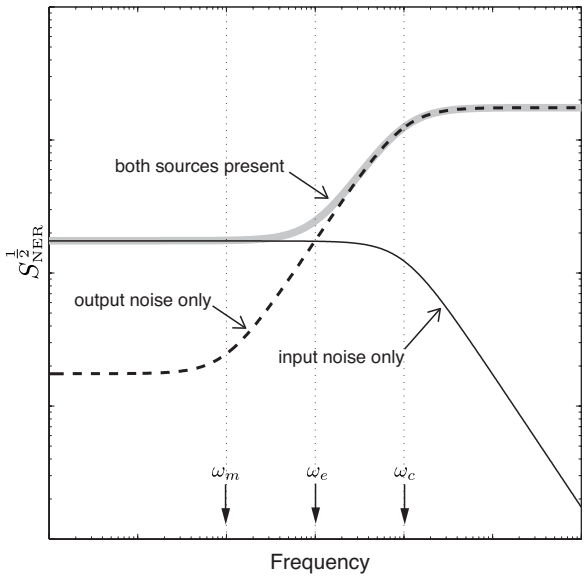


Fig. 3. NER spectrum for the three cases discussed in Sec. V-A. The double-sided spectra are shown for $\omega > 0$ and both axes have logarithmic scaling. For these plots $\nu_i \approx 10\nu_o/p$, so $\omega_e \approx 10\omega_m$. Furthermore, $\omega_c \approx 10\omega_e$.

*Output noise dominates.* When $\nu_i \to 0$, $\omega_e \to \omega_m$, the NER spectrum is

$$S_{\text{NER}}(\omega) = \frac{1}{2}\left(\frac{K_r}{\omega_c}\right)^2 \nu_o^2 \omega_c^2 \frac{\omega^2 + \omega_m^2}{\omega^2 + \omega_c^2}.$$

Since $\omega_c >> \omega_m$ by assumption, $S_{\text{NER}}$ has a phase-lead shape. The low frequency value is

$$S_{\text{NER}}(0) = \frac{1}{2}\left(\frac{\nu_o}{p}\right)^2, \tag{31}$$

and the high frequency asymptote is equal to (29). The spectrum is shown in Fig. 3 when the input noise is assumed to be zero.

### B. $S_{NER}(0)$ when $\Delta \neq 0$

The DC values of $S_{\text{NER}}$ are computed for the three cases introduced in Section V-A. In general,

$$S_{\text{NER}}(0) = \frac{1}{2}\left(\frac{K_r}{\omega_c}\right)^2 \nu_o^2 \left(\Delta^2 + \omega_e^2\right).$$

Despite the fact that $K_r$ and $\omega_c$ appear in $S_{\text{NER}}(0)$, under the assumption of large loop gain ($pK_r >> 1$), $S_{\text{NER}}(0)$ is independent of $K_r$ and $\omega_c$ and, hence, perturbations to these parameters have no impact on ARW.

*Input noise dominates.* In this case, $S_{\text{NER}}(0) = \frac{1}{2}\nu_i^2$ and because this expression is independent of $\Delta$, detuning does not increase the low frequency noise and (28) closely approximates the spectrum even if $|\Delta| \neq 0$. This conclusion differs from the result in [6] because it uses a different feedback scheme.

*No dominant noise source*. Both input and output noise sources are important and $S_{\text{NER}}(0)$ reduces to

$$S_{\text{NER}}(0) = \frac{1}{2}\left(\left(\frac{\nu_o}{p}\right)^2 + \nu_i^2\right)\left(1 + \left(\frac{\Delta}{\omega_e}\right)^2\right) \tag{32}$$

which is the value of $S_{\text{NER}}(0)$ when $\Delta = 0$ (refer to (30)) multiplied by the factor $1 + (\Delta/\omega_e)^2$. Note, however, if $|\Delta| < \omega_e$ then $S_{\text{NER}}(0)$ is not overly degraded. In other words, detuning up to the effective bandwidth can be tolerated without changing the spectrum of $S_{\text{NER}}$.

*Output noise dominates*. When the input noise can be ignored

$$S_{\text{NER}}(0) = \frac{1}{2}\left(\frac{\nu_o}{p}\right)^2\left(1 + \left(\frac{\Delta}{\omega_m}\right)^2\right)$$

which is the value of $S_{\text{NER}}(0)$ when $\Delta = 0$ (refer to (31)) multiplied by the factor $1 + (\Delta/\omega_m)^2$. This case exhibits the most sensitivity to detuning because if $|\Delta| > \omega_m$ (a situation that is inadvertently, though easily, achieved in high $Q$ sensors) then the ARW increases in proportion to the degree of detuning. Fig. 3 shows why the present case cannot tolerate as much detuning as the situation when neither noise source is dominant: when neither source is dominant $\omega_e > \omega_m$ and ARW does not appreciably change unless $|\Delta| > \omega_e$.

### C. Effect of changes in quality factor

The sense channel resonance quality factor ($Q$) and mechanical bandwidth, $\omega_m$, are inversely proportional. If all parameters in the resonator are held constant with the exception of $\omega_m$, the impact of quality factor on $S_{\text{NER}}$ can be determined for the previously discussed cases. This enables study of the "what if" scenario of changing the quality factor for a given sensor design. Note that the peak amplitude of $H_g$, $p$, is proportional to quality factor when all other parameters remain unchanged.

*Input noise dominates.* Recall $S_{\text{NER}}(0) = \frac{1}{2}\nu_i^2$. The source of the input noise $n_i$ may, or may not, depend on $Q$. If $S_{n_i}$ does not depend on $Q$ because it is due, for example, to external vibration that couples to the mode, then changes in $Q$ have no effect on $S_{\text{NER}}$. On the other hand, if $S_{n_i}$ is due to mechanical thermal noise, which is the case that has received the most attention in the MEM gyro literature, then $S_{n_i}$ has $Q^{-1}$ dependency so $S_{\text{NER}}(0)$ exhibits $Q^{-1}$ dependency.

*No dominant noise source.* Assume $\omega_m < \omega_e < \omega_c$ since this situation yields different results from the case when input noise dominates. Also assume $\Delta = 0$. Under these assumptions $S_{\text{NER}}$ has a phase-lead characteristic with $S_{\text{NER}}(0) = \frac{1}{2}((\nu_o/p)^2 + \nu_i^2)$. The high frequency asymptote is equal to $\frac{1}{2}(K_r\nu_o)^2$. Since $S_{n_o}$ models electrical buffer noise, it can be safely assumed that $\nu_o$ is independent of $Q$. Thus, the high frequency "knee" in $S_{\text{NER}}$ in Fig. 3 is unaffected by changes in $Q$ because $\omega_c$ and the high frequency asymptotic value are independent of the quality factor. The low frequency properties are affected by changes in $Q$, though. If $S_{n_i}$ is independent of $Q$, then, as $Q \to \infty$: 1) $S_{\text{NER}}(0)$ converges to the constant $\frac{1}{2}\nu_i^2$ because the higher $Q$ suppresses the output noise relative to the fixed input noise, and 2) the effective bandwidth $\omega_e$ decreases but converges to the non-zero constant $K_y K_f \nu_i/(2m\nu_0)$. If $S_{\text{NER}}(0)$ and $\omega_e$ are already close to these asymptotic values, further increase in $Q$ yields little reduction in ARW. On the other hand, if we assume $S_{n_i}$ is due to mechanical thermal noise, then increasing $Q$ will preferentially reduce the effect of $\nu_o$ compared to $\nu_i$, and $S_{\text{NER}}(0)$ converges to $\frac{1}{2}\nu_i^2$, which has $Q^{-1}$ dependency.

*Output noise dominates.* This is an interesting case because $S_{\text{NER}}$ has the greatest sensitivity to $Q$. Recall $S_{\text{NER}}(0) = \frac{1}{2}(\nu_o/p)^2$, where $p$ is the peak gain of the open-loop frequency response. Because $p$ is proportional to $Q$, $S_{\text{NER}}(0)$ has $Q^{-2}$ dependency and the value of low frequency corner in the spectrum at $\omega_m$ has $Q^{-1}$ dependency. Although this greater sensitivity is desirable it does come with a price, namely, to reap the benefits of high $Q$, the degree of permissible detuning must satisfy $|\Delta| < \omega_m$, which can be difficult to achieve in practice. As in case when neither noise source is dominant, the high frequency corner and asymptotic value of $S_{\text{NER}}$ do not depend on $Q$.

### D. Comparison with open-loop sensor

It will be shown that $S_{\text{NER}}(0)$ is the same in both the open- and closed-loop sensor assuming that the physical mechanism which implements the feedback does not contribute any noise. A meaningful comparison can only be made when $\Delta = 0$ ($\omega_0 = \omega_n$) because the open-loop sensor scale factor exhibits first order dependence on $\Delta$ whereas the closed-loop scale factor is essentially independent of $\Delta$. It's useful to retain the notation introduced for the closed-loop analysis so the open-loop sensor is analyzed by breaking the loop at the point indicated in Fig. 2. The signal $d$ is still demodulated to recover the rate estimate and so its spectral properties due to the input and output noises will govern the NER for the open-loop case. The spectrum of $d$ in the open-loop case is

$$S_{d,\text{OL}}(\omega) = K_r^2\left(S_{n_o} + |H_g(\omega)|^2 S_{n_i}\right).$$

To follow the closed-loop analysis $d$ should be multiplied by the amplitude of the demodulating drive signal (which is assumed to be the same as the closed-loop sensor) and normalized by the *open-loop* scale factor $\gamma_{\text{OL}}$. In other words, the scaled signal is defined $\tilde{d} := (K_x a\omega_n/\gamma_{\text{OL}})d$ so

$$S_{\tilde{d},\text{OL}}(\omega) = \left(\frac{K_x a\omega_n}{\gamma_{\text{OL}}}\right)^2 K_r^2\left(S_{n_o} + |H_g(\omega)|^2 S_{n_i}\right).$$

The open-loop scale factor differs from the closed-loop scale factor, however, the following relation can be derived

$$\frac{1}{\gamma_{\text{OL}}} = \frac{1}{1 + pK_r}\frac{1}{\gamma_0},$$

where $\gamma_{\text{OL}}$ is the open-loop scale factor, and $\gamma_0$ is the nominal scale factor of the closed-loop sensor when $\Delta = 0$ (see (10)). Substituting this expression into $S_{\tilde{d}}$ yields

$$\begin{aligned} S_{\tilde{d},\text{OL}}(\omega) &= \left(\frac{K_x a\omega_n}{\gamma_0}\right)^2\left(\frac{K_r}{1 + pK_r}\right)^2\left(S_{n_o} + |H_g(\omega)|^2 S_{n_i}\right) \\ &= \left(\frac{K_r}{1 + pK_r}\right)^2\left(\nu_o^2 + |H_g(\omega)|^2\nu_i^2\right), \end{aligned}$$

where $\nu_o$ and $\nu_i$ retain the same definitions from the closed-loop analysis (see (14)). The open-loop NER spectrum at $\omega = 0$ is

$$S_{\text{NER,OL}}(0) = \frac{1}{2}S_{\tilde{d},\text{OL}}(\omega_n) = \frac{1}{2}\left(\frac{K_r}{1 + pK_r}\right)^2\left(\nu_o^2 + p^2\nu_i^2\right),$$

where we have used the fact that $|H_g(\omega_n)| = p$. Since the open-loop sensor is compared to the closed-loop case under the large loop gain assumption $pK_r >> 1$, then $K_r/(1+pK_r) \approx 1/p$ so the spectral density reduces to

$$S_{\text{NER,OL}}(0) = \frac{1}{2}\frac{1}{p^2}\left(\nu_o^2 + p^2\nu_i^2\right).$$

which is equal to the closed-loop NER spectrum given by (30). Thus, the ARW associated with closed-loop sensor is equal to the ARW associated with the open-loop sensor. This result comes as no surprise because feedback does not change the signal-to-noise ratio of the pick-off signal $\tilde{y}$ in Fig. 2.

### *E. Asymptotes for $\sigma_\tau^2$*

Asymptotes for $\sigma_\tau^2$ are developed for the three scenarios and although it was demonstrated in Sec. V-D that $S_{\text{NER}}(0)$, which defines the sensor's ARW, is the same for the open- and closed-loop sensor, the fact that $\sigma_\tau^2$ is a weighted integral of $S_{\text{NER}}$ means that $\sigma_\tau^2$ has additional features that can be attributed to the presence of output noise. The asymptotes are derived under the condition $\Delta = 0$.

*Input noise dominates.* The variance expression (24) reduces to

$$\sigma_\tau^2 = \frac{1}{2}\nu_i^2\left(\tau - \frac{1}{\omega_c}\left(1 - e^{-\omega_c\tau}\right)\right) \tag{33}$$

when $\nu_o \to 0$. The situation $\tau < 1/\omega_c$ has little practical relevance because the integration time is shorter than the closed-loop time constant. The relevant situation is $\tau > 1/\omega_c$ and (33) is approximated by

$$\sigma_\tau^2 = \frac{1}{2}\nu_i^2\tau, \quad (\tau > 1/\omega_c),$$

This is the classical ARW trend in which the variance grows proportionally with the integration time for integration times exceeding the closed-loop time constant. It will be shown that this trend does not hold for all $\tau > 1/\omega_c$ when output noise must be included in the analysis.

*No dominant noise source.* It is assumed $\omega_e < \omega_c$ because, if not, the present case is well-approximated by the case when input noise dominates. The variance

$$\sigma_\tau^2 = \frac{1}{2}\left(\frac{K_r}{\omega_c}\right)^2\nu_o^2\left(\omega_e^2\tau + \frac{\omega_c^2 - \omega_e^2}{\omega_c}\left(1 - e^{-\omega_c\tau}\right)\right).$$

has three distinct trends

$$\sigma_\tau^2 \approx \begin{cases} \frac{1}{2}K_r^2\nu_o^2\tau, & \tau < 1/\omega_c \\ \frac{1}{2}K_r^2\nu_o^2/\omega_c, & 1/\omega_c < \tau < \omega_c/\omega_e^2 \\ \frac{1}{2}\left((\nu_o/p)^2 + \nu_i^2\right)\tau, & \tau > \omega_c/\omega_e^2. \end{cases}$$

The relevant integration times are those greater than $1/\omega_c$ and it is observed that two asymptotes define $\sigma_\tau^2$. In particular, if $\tau \in [1/\omega_c, \omega_c/\omega_e^2]$, then the variance is *independent* of $\tau$, in other words, *angle white noise* (AWN) dominates this integration range and $\sigma_\tau^2$ is proportional to $\nu_o^2$ and to $K_r$. On the other hand, if $\tau > \omega_c/\omega_e^2$, then the ARW asymptote defined by $S_{\text{NER}}(0)$ in (30) determines $\sigma_\tau^2$. The price of increasing the sensor's bandwidth becomes evident: if $\omega_c/\omega_e^2 > 1/\omega_m$, the closed-loop sensor, while having superior bandwidth compared to the open-loop sensor, has larger variance for those integration times relevant to both open- and closed-loop modes of operation, namely when $\tau > 1/\omega_m$. This is shown as the cross-hatched region in Fig. 4. Note, however, that $\sigma_\tau$ does converge to the open-loop value as $\tau$ increases beyond $\omega_c/\omega_e^2$.

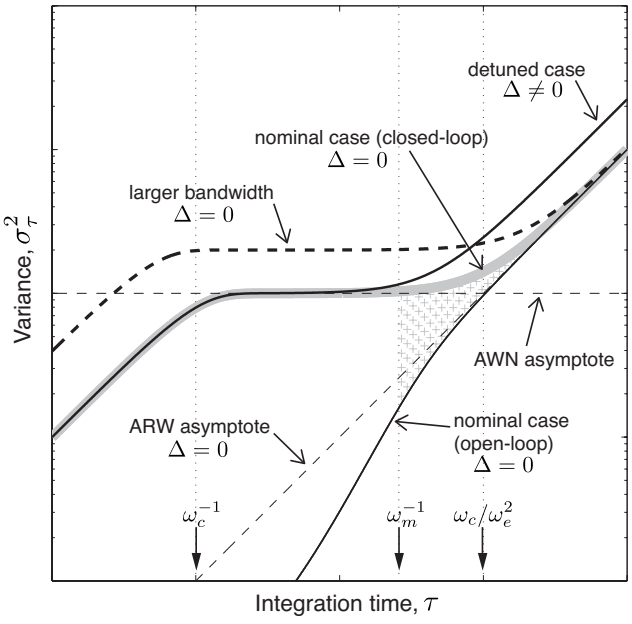


Fig. 4. Angle variance versus $\tau$ when neither noise source is dominant. Logarithmic axes are used. ARW and AWN asymptotes of the nominal tuned closed–loop case are plotted with dashed lines. The tuned closed–loop plots converge to the tuned open–loop variance as $\tau \to \infty$. When $|\Delta| > \omega_e$, though, the ARW asymptote increases. If the closed–loop bandwidth is increased when $\Delta = 0$, $\sigma_\tau$'s AWN asymptote increases in proportion to the square root of the closed–loop bandwidth, however, the ARW asymptote is unchanged. The cross-hatch region denotes the integration times for which the closed-loop sensor produces larger variance than the open loop sensor (the comparison is made for $\tau > 1/\omega_m$, which is the time constant of the open-loop sensor). When output noise dominates, $\omega_e$ is replaced with $\omega_m$. The closed-loop angle variance when input noise dominates is simply the dashed line denoted "ARW asymptote."

*Output noise dominates.* The asymptotes in previous case apply with $\omega_e$ replaced by $\omega_m$,

$$\sigma_\tau^2 \approx \begin{cases} \frac{1}{2}K_r^2\nu_o^2\tau, & \tau < 1/\omega_c \\ \frac{1}{2}K_r^2\nu_o^2/\omega_c, & 1/\omega_c < \tau < \omega_c/\omega_m^2 \\ \frac{1}{2}(\nu_o/p)^2\tau, & \tau > \omega_c/\omega_m^2 \end{cases}.$$

The closed-loop sensor exhibits larger variance than the open-loop sensor when $\tau \in [1/\omega_m, \omega_c/\omega_m^2]$, but, as $\tau$ increases beyond $\omega_c/\omega_m^2$, $\sigma_\tau^2$ converges to the open-loop ARW.

## VI. Experimental Results

This section compares predictions of the $S_{\text{NER}}$ and $\sigma_\tau$ models to experimental data from a Disk Resonator Gyro (DRG). Details of the DRG can be found in [5] with the control loop design discussed at length in [7]. The basic sensor has two forcers and two pick-offs, denoted $(d_1, d_2)$ and $(s_1, s_2)$, from which four scalar-valued frequency response functions can be measured as shown in Fig. 5. The sensor can be configured for

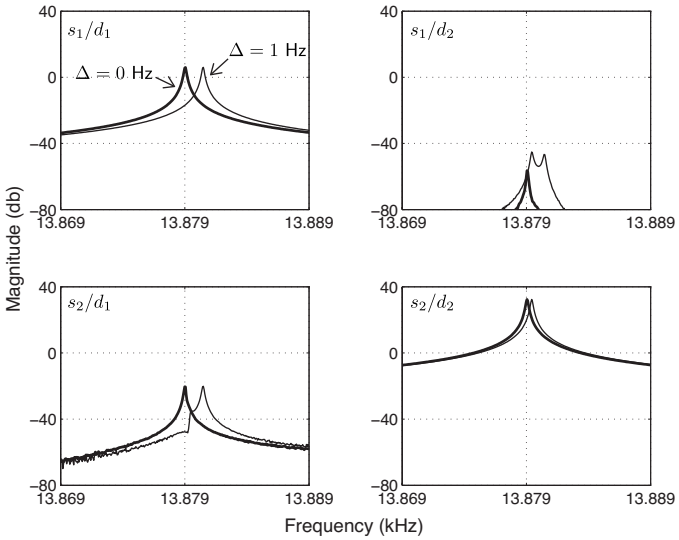


Fig. 5. Empirical frequency response of all channels of the open-loop DRG. The four transfer function magnitudes are represented in these plots. The $s_1/d_1$ channel modal frequency determines $\omega_0$ while the $s_2/d_2$ channel frequency determines $\omega_n$. The tuned state, i.e. $\Delta \approx 0$, is represented with the thick line. Experiments are also performed with the sensor in a detuned state in which $\Delta \approx 1$ Hz –this case is represented by the thin line where it is observed $\omega_0 - \omega_n \approx 1$ Hz. The off-diagonal channels represent coupling between the two degrees of freedom. The coupling is the source of angular rate and quadrature bias, and instability in the angular rate bias can contribute to $S_{\text{NER}}$, however, coupling effects are neglected in the present analysis.

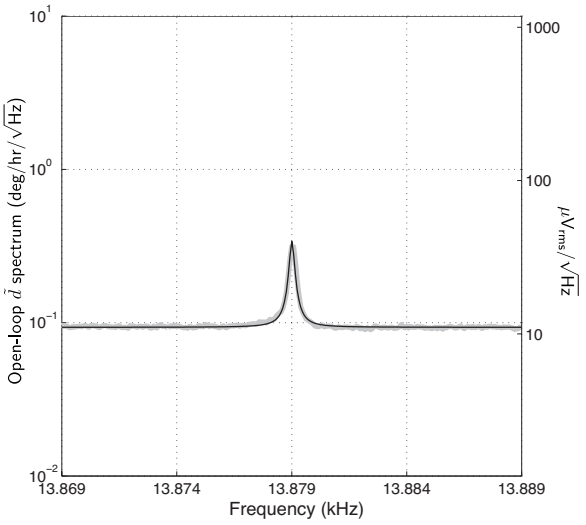


Fig. 6. Open–loop noise spectrum of $\tilde{d}$. The model fit (black, thin line) to the measured data (gray, thick line) estimates the input and output noise intensities as $\nu_i = 0.33\text{deg/hr}/\sqrt{\text{Hz}}$ and $\nu_o = 3.9\text{deg/hr}/\sqrt{\text{Hz}}$, respectively. The effective bandwidthh is $\omega_e = 0.38$ Hz.

tuned or detuned operation, also shown in Fig. 5. The $s_1/d_1$ transfer function is used for designing the excitation loop so the frequency of the resonance in this channel establishes $\omega_0$. The $s_2/d_2$ channel represents $H_g$ in the analysis and the frequency of the resonance in this channel defines $\omega_n$. Although the formulae in Sec. III and IV require all frequency parameters to be expressed in units of radians/second for computation, the frequency parameters in this section are given in units of hertz. The following sense channel parameters are noted for the tuned sensor: $\omega_0 = \omega_n = 13879$ Hz, $\omega_m = 0.104$ Hz (Q = 66.7K), and $p = 41.6$. The sense loop is closed with rebalance gain $K_r = 2.5$, which yields closed-loop bandwidth $\omega_c \approx 10$ Hz. The low-pass filters used after signal demodulation have corner frequency $\omega_{lp} = 62.5$ Hz. Note that the assumptions made for the derivation of (18) are satisfied with these sensor parameters. The (open-loop) noise spectrum of the sense pick-off is shown in Fig. 6. After measurement of the closed-loop scale factor and the demodulating signal amplitude, the voltage noise spectrum is scaled to angular rate units and the parameters selected $\nu_i = 0.33\,\text{deg/hr}/\sqrt{\text{Hz}}$, $\nu_o = 3.9\,\text{deg/hr}/\sqrt{\text{Hz}}$ in the open-loop noise model $\nu_0^2 + |H_g|^2\nu_i^2$. The effective bandwidth associated with this noise model is $\omega_e = 0.38$ Hz. Note that $\omega_m < \omega_e < \omega_c$ so neither noise source dominates, i.e. the analysis must include both input and output noise for accurate prediction of $S_{\text{NER}}$.

Prior to comparing measured NER spectrum to those predicted by the model, the sensor frequency response when $\omega_c = 10$ Hz and $\Delta \approx 0$ and $\Delta \approx 1$ Hz are measured – see Fig. 7. The frequency response is generated by correlating the sensor output with the measured angular rate from the rate table controller. The nominal scale factor $\gamma_0$ was computed for the case $\Delta \approx 0$ so it is expected that DC gain associated with its frequency response is 0dB as is evident in the figure. This scale factor, however, is also used in the measurement of the frequency response when $\Delta \approx 1$ Hz so that fact that the frequency response for this case also has DC gain of 0dB demonstrates the insensitivity of $\gamma$ to detuning. Furthermore, the transfer function corner frequency is also robust to detuning.

Estimates of $S_{\text{NER}}$ are obtained by acquiring twenty four hours of contiguous angular rate data at a sample rate of 156.25 Hz and under the condition $\Omega = 0$. A separate experiment was conducted for every estimate of $S_{\text{NER}}$ shown in the subsequent figures. Long term changes in the $\Omega_e$ bias value are due to slowly changing sensor dynamics over the twenty four hour acquisition period so a 2-pole high-pass filter with 0.0003 Hz corner frequency detrends the raw angular rate measurement. The NER spectra are calculated by applying Welch's method to the detrended data with a subrecord length of $2^{15}$ points (corresponding to averaging the spectra obtained from subrecords of 210 second duration) [16]. When computing $\sigma_\tau$, the detrended time domain data are directly analyzed. In other words, the recorded angular rate data is split into non-overlapping $\tau$-second subrecords, the subrecords are integrated, then, the variance of the integrated values is determined.

It is of interest to see how the model (18) compares to the NER spectrum computed from the measured angular rate data. For this exercise the basic sensor parameters $\{\omega_0, \omega_m, \omega_n, p\}$ along with the desired closed-loop bandwidth $\omega_c$ are used to compute $\{\Delta, K_r\}$. The only required closed-loop measurement is the scale factor, $\gamma_0$. It is also necessary to measure the open-loop noise spectrum at the pick-off to estimate $\{\nu_o, \nu_i\}$, then, $\omega_e$ can be computed. Thus, the

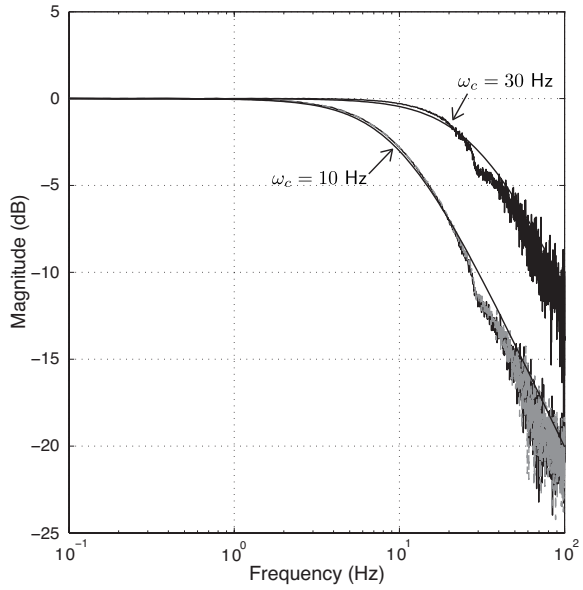


Fig. 7. Closed-loop frequency response magnitude when $\omega_c = 10$ Hz and $\omega_c = 30$ Hz. For the 10 Hz case, $\Delta \approx 0$ Hz (black) and $\Delta \approx 1$ Hz (grey). The thin black line is the magnitude of $1/(s/(10 \cdot 2\pi) + 1)$. For the 30 Hz case, only measurements when $\Delta = 0$ are shown, and the thin black line is the magnitude of the model $1/(s/(30 \cdot 2\pi) + 1)$. The transfer functions are identified by correlating the rate table angular rate with the sensor output using the *same* nominal scale factor $\gamma_0$ for all cases (corresponding to a measurement made on the 30 Hz bandwidth sensor). Note that when $\omega_c = 10$ Hz and $\Delta = 0$, the DC gain is equal to the $\omega_c = 30$ Hz case. Furthermore, the DC gain remains unchanged even when $\Delta \approx 1$ Hz. These tests demonstrate that $\gamma_c$ is independent of $K_r$ and $\Delta$ which justifies the use of $\gamma_0$ in all measurements.

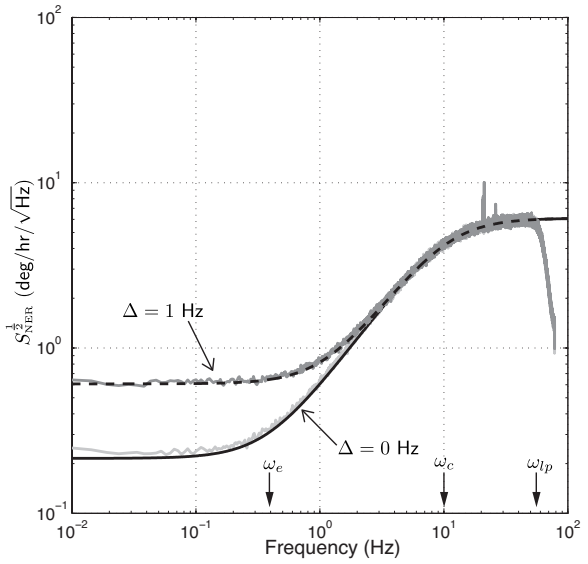


Fig. 8. Comparison of $S_{\text{NER}}$ for the $\Delta \approx 0$ and $\Delta \approx 1$ Hz, 10 Hz bandwidth cases. The model predictions are shown in the solid black and dashed black traces. The detuning is larger than the effective bandwidth so the low frequency noise floor increases by the factor $\sqrt{(\Delta/\omega_e)^2 + 1} = 2.8$ as derived in (32). The high frequency corner at $\omega_c$ and the high frequency asymptotic value of $S_{\text{NER}}$ are unaffected by detuning. The anti-alias filter constrains the bandwidth of $S_{\text{NER}}$ to the interval $[-\omega_{lp}, \omega_{lp}]$ where $\omega_{lp} = 62.5$ Hz. The $S_{\text{NER}}$ model does not include the anti-alias filter.

parameters $\{\nu_o, \omega_e, \Delta, K_r, \omega_c\}$ are substituted into (18) to yield predictions of the closed-loop NER spectra. The model predictions are compared to the measurements in Fig. 8 when $\Delta \approx 0$ and $\Delta \approx 1$ Hz (the double sided spectral densities are graphed only for $\omega > 0$). Note that $\omega_m < \omega_e < \omega_c$ so neither noise source is dominant and, hence, the analysis of Sec. V-B can be applied. When $\Delta \approx 1$ Hz, $S_{\text{NER}}^{\frac{1}{2}}(0)$ is expected to increase by the factor $\sqrt{(\Delta/\omega_e)^2 + 1} = 2.8$ and this is seen to be the case in Fig. 8. The model predicts $S_{\text{NER}}$ quite accurately, however, the anti-alias filter that rolls off at $\omega_{lp}$ is not included in the analysis.

The effect of the changes in the rebalance gain $K_r$ are shown in Fig. 9. In this comparison $K_r$ increases by a factor of three –from 2.5 to 7.3. The analysis shows that the corner frequency $\omega_c$ and the asymptotic value of $S_{\text{NER}}^{\frac{1}{2}}$ are proportional to $K_r$ so they also experience an increase by a factor of three. In fact, $\omega_c$ increases from about 10 Hz to 30 Hz and the high frequency asymptotic value of $S_{\text{NER}}^{\frac{1}{2}}$ increases from about $6$ deg/hr/$\sqrt{\text{Hz}}$ to $18$ deg/hr/$\sqrt{\text{Hz}}$. The low frequency noise floor is insensitive to the change in $K_r$. Although $\Delta \approx 0$ in this comparison, $\Delta$ does not effect the high frequency asymptotic value or its corner frequency (see Fig. 8).

Two experiments are also performed by manipulating $\omega_e$. The sensor was exposed to narrow band random vibration via a modal shaker such that the disturbance had a flat passband extending from 13.829 kHz to 13.929 kHz. The case vibration couples to the sensor modes and can be modeled as an increase

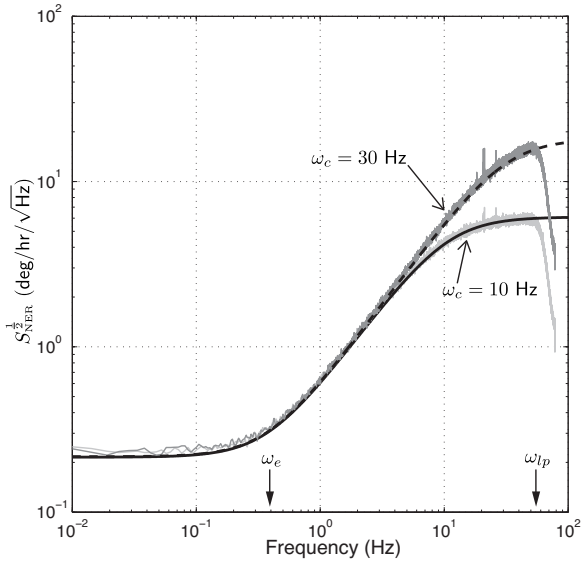


Fig. 9. Comparison of $S_{\text{NER}}$ when $\Delta \approx 0$ but with $\omega_c = 10$ Hz and $\omega_c = 30$ Hz (see Fig. 7). The model predictions are shown in the solid black and dashed black traces. Different bandwidths are achieved by changing the rebalance gain $K_r$. It is evident that $S_{\text{NER}}(0)$ is independent of $K_r$, however, since $K_r$ is increased by about a factor of three, the closed-loop corner frequency $\omega_c$ also increases by the same factor (as indicated by (5)) and so does the high frequency asymptotic value of $S_{\text{NER}}^{\frac{1}{2}}$ (as implied by (29)).

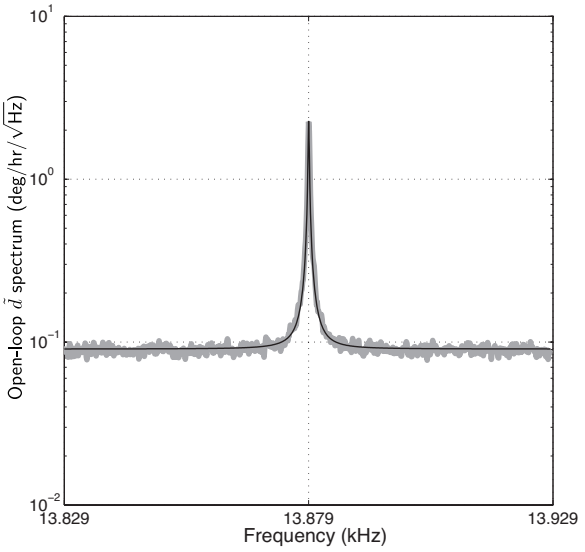


Fig. 10. Open–loop noise spectrum when an input disturbance (sensor case vibration) is applied. The thin black trace is the open-loop noise model with $\nu_o = 3.9\,\text{deg/hr}/\sqrt{\text{Hz}}$ and $\nu_i = 2.3\,\text{deg/hr}/\sqrt{\text{Hz}}$. Note that $\nu_i$ has increased compared to the spectrum in Fig. 6. The new effective bandwidth is $\omega_e = 2.5\,\text{Hz}$.

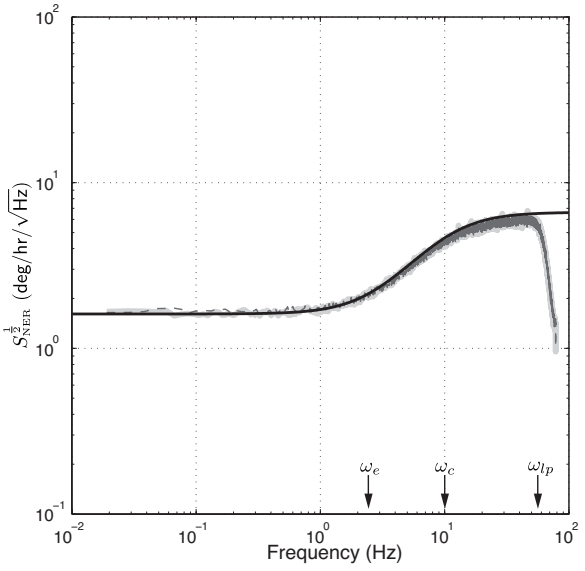


Fig. 11. $S_{\text{NER}}$ when $\Delta \approx 0$ Hz and $\Delta \approx 1$ Hz for the open-loop spectrum in Fig. 10. The effective bandwidth is larger than $|\Delta|$ in both cases, though, so no change is observed in the spectra (compare with Fig. 8). The model with $\Delta = 0$ is shown as the solid black line, the experiment with $\Delta \approx 0$ is shown as the thick gray line, and the experiment with $\Delta \approx 1\,\text{Hz}$ is shown as the dashed line.

in the value of $\nu_i$ –note that $\nu_o$ remains fixed because the signal conditioning electronics are unmodified. The new open-loop spectrum is shown in Fig. 10. The effective bandwidth has increased from $0.38\,\text{Hz}$ to $2.5\,\text{Hz}$. The same detuning experiments are conducted with $\Delta \approx 0\,\text{Hz}$ and $\Delta \approx 1\,\text{Hz}$ but in both cases $|\Delta| < \omega_e$ so no impact is observed in $S_{\text{NER}}$ as shown in Fig. 11.

Lastly, Figs. 12 and 13 display $\sigma_\tau$ calculated from the same detrended angular rate data that was used to compute the

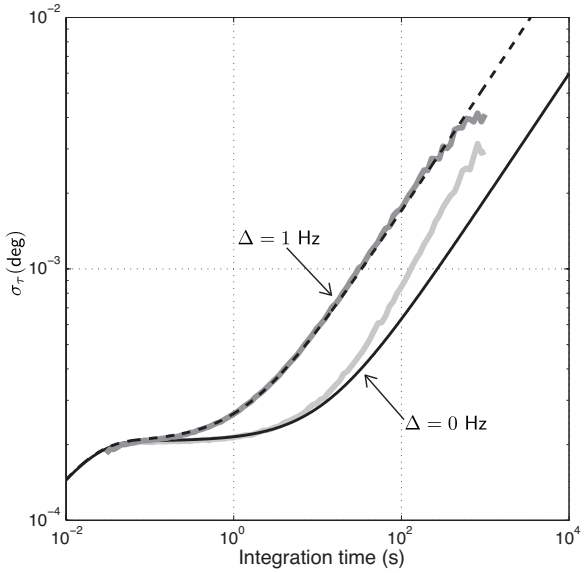


Fig. 12. The angular rate data used to produce the spectra in Fig. 8 is also used to compute $\sigma_\tau$, shown here along with the model predictions (the thin solid and dashed lines). Note that $\omega_c$ remains fixed at 10 Hz for each case. When $\Delta \approx 0$, the ARW trend at longer integration times does not match the model prediction because drift in the angular rate bias contributes low frequency power to $S_{\text{NER}}$. When the sensor is detuned, though, the increase in low frequency power due to the noise sources dominates the power contributed by the bias drift, so the model prediction and data are almost indistinguishable in this case. Note that the AWN asymptote is not effected by detuning, although the $\tau$ interval over which AWN dominates will change.

spectra in Figs. 8 and 9. The predictions of $\sigma_\tau$ using (24) are also shown. As the modes detune, the increase in the value of the angle random walk asymptote is evident in Fig. 12. On the other hand, if $\Delta \approx 0$ but the closed–loop bandwidth is increased, then the AWN increases as shown in Fig. 13. The factor of three increase in closed-loop bandwidth produces a $\sqrt{3}$ increase in $\sigma_\tau$'s AWN. The long-term trend in $\sigma_\tau$ in Figs. 12 and 13 do not precisely follow the ARW asymptotes calculated from the model for the $\Delta \approx 0$ experiments. This is caused by drift in the zero-rate bias over the 24 hour test period. The bias drift is due not to changes in the noise sources but rather subtle changes in the sensor dynamics. The bias drift adds low frequency power to $S_{\text{NER}}$ that is not completely removed by the detrending filter. In fact, the empirical $S_{\text{NER}}$ plots in Figs. 8 and 9 associated with the $\Delta \approx 0$ cases show slightly higher power at lower frequencies compared to the asymptote predicted by the model based on the open-loop noise spectra. In the detuned case, though, the value of $S_{\text{NER}}(0)$ is increased to such an extent that the added power from the bias drift is masked so in this case the ARW asymptote and data are coincident.

The bias drift is also evident in the Allan deviation plot for the $\Delta \approx 0$ and $\Delta \approx 1$ Hz, 10 Hz bandwidth cases shown in Fig. 14. The Allan variance model (26) predicts the data quite well except at longer integration times where instability in the zero rate bias (which is not modeled) becomes the dominant trend.

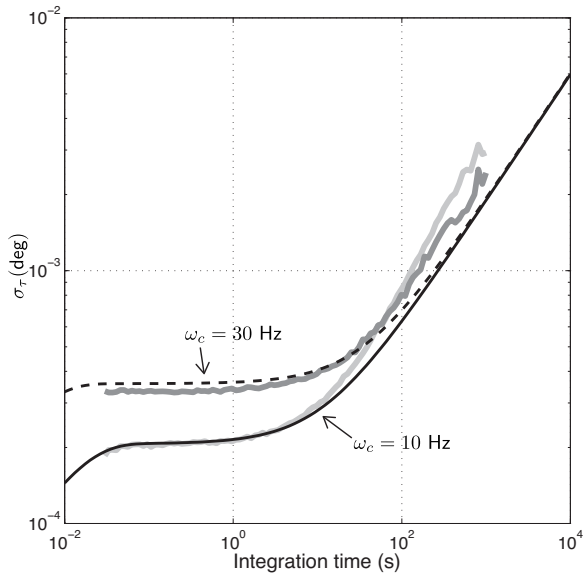


Fig. 13. The data used to create the spectra in Fig. 9 is analyzed to compute $\sigma_\tau$. Note $\Delta \approx 0$ Hz for each case, however, the sensor bandwidth is changed. Increasing the bandwidth produces larger AWN. The model (shown as the solid and dashed black traces) over-predicts the measured AWN because the anti-alias filter attenuates $S_{\text{NER}}$ above $\omega_{lp}$ (this can be corrected by constraining the integral in (21) to the range $[-\omega_{lp}, \omega_{lp}]$).

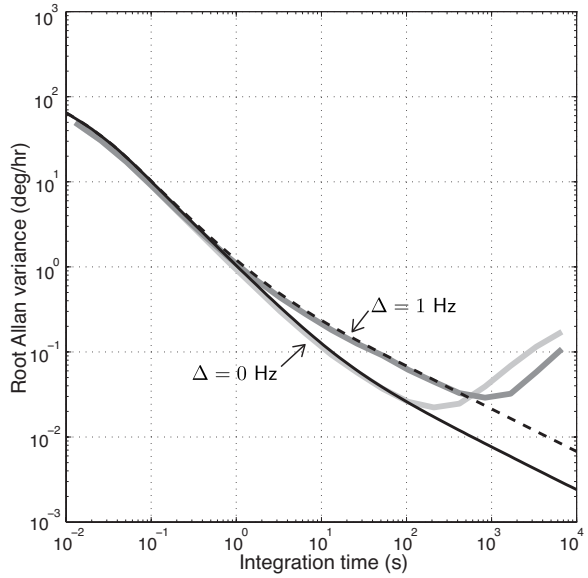


Fig. 14. The square root of the Allan variance computed from the time domain data and its comparison to prediction of the model in (26) for the $\Delta \approx 0$ and $\Delta \approx 1$ Hz, 10 Hz bandwidth cases are shown in this figure. The model predictions are shown in the solid black and dashed black traces. At longer integration times ramping in the zero rate bias causes the Allan variance to increase and depart from the model prediction.

## VII. Conclusion

Comprehensive noise analysis of a closed–loop vibratory rate gyro has been developed with regard to input and output noise sources. The effective bandwidth parameter was introduced to capture the relative power of the input noise versus output noise. In all scenarios, the low frequency asymptote of $S_{\text{NER}}$ determines the ARW, thus, it is important to minimize the value of this asymptote and it was shown that if the sensor modes are detuned beyond the effective bandwidth an increase in the low frequency asymptote of $S_{\text{NER}}$ will occur. The analysis also shows that if output noise can be neglected, detuning has no impact on ARW, however, if output noise is the dominant source, then the effective bandwidth is close to the mechanical bandwidth and the ARW figure is very sensitive to detuning. It was also demonstrated that the closed-loop sensor retains the same value of $S_{\text{NER}}(0)$ as the open-loop sensor ($\Delta = 0$ in both cases), so feedback does not change the ARW figure but despite this fact, analysis of the variance of the integrated rate shows for the closed-loop sensor, that output noise creates angle white noise which produces larger variance of the integrated signal compared to what would be obtained with the open loop sensor. This result can be used to precisely quantify both the benefits and potential drawbacks of operating the sensor in closed-loop. The experimental results with a Disk Resonator Gyro showed very close agreement with the model predictions, however, drift in the zero rate bias adds power to the low frequency spectrum and causes deviation of the long-term measured angle variance from the ARW figure predicted by the model. This underscores a real challenge, namely, pushing the quality factors to ever higher values does not necessarily translate into improved performance unless a means can be found to stabilize the sensor dynamics so that the noise power created by bias drift does not dominate the low frequency behavior of $S_{\text{NER}}$.

## Appendix

The integral $I$ is evaluated using the contour shown in Fig. 15. The contour orientation is counterclockwise. The integrand of $I$ is extended to the complex-valued function $f$ of the complex variable $z$

$$f(z) := \frac{\left(\Delta^2 + \omega_c^2 + z^2\right)\left(\Delta^2 + \omega_e^2 + z^2\right) - (2\Delta z)^2}{\left((\Delta - z)^2 + \omega_c^2\right)\left((\Delta + z)^2 + \omega_c^2\right)} \cdot \frac{2}{z^2}\left(1 - e^{j\tau z}\right), \quad z \in \mathbb{C}.$$

Note that $f$ is analytic at all points with the exception of its poles. The poles of $f$ inside the contour are $\{\Delta + j\omega_c, -\Delta + j\omega_c\}$ so

$$\int_\rho^R f(z)dz + \int_{C_R} f(z)dz + \int_{-R}^{-\rho} f(z)dz + \int_{C_\rho} f(z)dz = 2\pi j\left(\text{Res}(f, \Delta + j\omega_c) + \text{Res}(f, -\Delta + j\omega_c)\right) \tag{34}$$

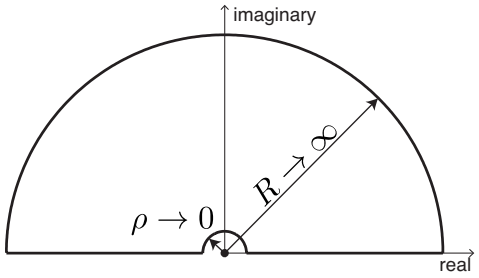


Fig. 15. Contour for evaluating (23).

where $\mathrm{Res}(f, z_0)$ denotes the residue of $f$ at $z_0 \in \mathbb{C}$. The restriction of $f$ to $z \in \mathbb{R}^+$, i.e. $z = \omega > 0$, is equal to

$$f(\omega) = \frac{\left(\Delta^2 + \omega_c^2 + \omega^2\right)\left(\Delta^2 + \omega_e^2 + \omega^2\right) - (2\Delta\omega)^2}{\left((\Delta - \omega)^2 + \omega_c^2\right)\left((\Delta + \omega)^2 + \omega_c^2\right)} \cdot \frac{2}{\omega^2}\left(1 - \cos(\tau\omega) - j\sin(\tau\omega)\right),$$

so the real part of $f$ in this case is equal to the integrand of $I$. Furthermore, since $f(-\omega)$ is the complex conjugate of $f(\omega)$, then $I$ can be computed as a Cauchy principal value,

$$I = \lim_{\substack{\rho \to 0 \\ R \to \infty}} \int_{\rho}^{R} f(z)dz + \int_{-R}^{-\rho} f(z)dz.$$

Since

$$\lim_{|z| \to \infty} |f(z)| = 0, \quad \text{(uniformly)}$$

then by Jordan's Lemma

$$\lim_{R \to \infty} \int_{C_R} f(z)dz = 0$$

so (34) reduces to

$$I + \lim_{\rho \to 0} \int_{C_\rho} f(z)dz = 2\pi j\left(\mathrm{Res}(f, \Delta + j\omega_c) + \mathrm{Res}(f, \Delta - j\omega_c)\right).$$

The evaluation of the integral on $C_\rho$ yields

$$\lim_{\rho \to 0} \int_{C_\rho} f(z)dz = -\frac{\Delta^2 + \omega_e^2}{\Delta^2 + \omega_c^2} 2\pi\tau.$$

The residues are

$$\mathrm{Res}(f, \Delta + j\omega_c) = \frac{\omega_e^2 - \omega_c^2}{j2\omega_c\left(\Delta + j\omega_c\right)^2}\left(1 - e^{-\tau\omega_c + j\tau\Delta}\right)$$

$$\mathrm{Res}(f, -\Delta + j\omega_c) = \frac{\omega_e^2 - \omega_c^2}{j2\omega_c\left(\Delta - j\omega_c\right)^2}\left(1 - e^{-\tau\omega_c - j\tau\Delta}\right).$$

Gathering these results yields

$$I = 2\pi\frac{\Delta^2 + \omega_e^2}{\Delta^2 + \omega_c^2}\tau + 2\pi\frac{\omega_c^2 - \omega_e^2}{\omega_c(\Delta^2 + \omega_c^2)^2} \cdot \left(\left(\omega_c^2 - \Delta^2\right)\left(1 - \cos(\Delta\tau)e^{-\omega_c\tau}\right) + 2\Delta\omega_c\sin(\Delta\tau)e^{-\omega_c\tau}\right).$$

Substituting $I$ into (22) yields the closed-form expression for $\sigma_\tau^2$.

## ACKNOWLEDGMENT

The authors wish to thank the Defense Advanced Research Projects Agency micro-PNT program for financial support.

## REFERENCES

[1] A. Lawrence, *Modern Inertial Technology: Navigation, Guidance, and Control*. New York: Springer-Verlag, 1993.

[2] T. Gabrielson, "Mechanical-thermal noise in micromachined acoustic and vibration sensors," *IEEE Trans. Electron Devices*, vol. 40, no. 5, pp. 903 – 909, May 1993.

[3] D. D. Lynch, "Vibration-induced drift in the hemispherical resonator gyro," in *Proc. Annual Meeting of the Institute of Navigation*, Dayton, Ohio, June 1987.

[4] J. B. Johnson, "Thermal agitation of electricity in conductors," *Physical Review*, vol. 32, pp. 97 – 109, July 1928.

[5] A. To, W. Liu, G. Olson, T. Belytschko, W. Chen, M. Shephard, Y.-W. Chung, R. Ghanem, P. Voorhees, D. Seidman, C. Wolverton, J. Chen, B. Moran, A. Freeman, R. Tian, X. Luo, E. Lautenschlager, and A. Challoner, "Materials integrity in microsystems: a framework for a petascale predictive-science-based multiscale modeling and simulation system," *Computational Mechanics*, vol. 42, pp. 485 – 510, 2008.

[6] R. P. Leland, "Mechanical–thermal noise in mems gyroscopes," *IEEE Sensors J.*, vol. 5, no. 3, pp. 493–500, 2005.

[7] D.-J. Kim and R. T. M'Closkey, "Dissecting tuned mems vibratory gyros," in *Feedback Control of MEMS to Atoms*, J. J. Gorman and B. Shapiro, Eds. Springer, 2012.

[8] Y.-C. Chen, R. T. M'Closkey, T. Tran, and B. Blaes, "A control and signal processing integrated circuit for the jpl-boeing micromachined gyroscopes," *IEEE Trans. Control Syst. Technol.*, vol. 13, no. 2, pp. 286 – 300, 2005.

[9] J. Raman, E. Cretu, P. Rombouts, and L. Weyten, "A closed-loop digitally controlled mems gyroscope with unconstrained sigma-delta force-feedback," *IEEE Sensors J.*, vol. 9, no. 3, pp. 297 – 305, March 2009.

[10] V. Petkov and B. Boser, "High-order electromechanical $\Sigma\Delta$ modulation in micromachined inertial sensors," *IEEE Trans. Circuits Syst. I, Reg. Papers*, vol. 53, no. 5, pp. 1016 – 1022, May 2006.

[11] M. Palaniapan, R. Howe, and J. Yasaitis, "Performance comparison of integrated z-axis frame microgyroscopes," in *Micro Electro Mechanical Systems, 2003. MEMS-03 Kyoto. IEEE The Sixteenth Annual International Conference on*, Jan. 2003, pp. 482 – 485.

[12] M. Weinberg and A. Kourepenis, "Error sources in in-plane silicon tuning-fork mems gyroscopes," *J. Microelectromech. Syst.*, vol. 15, no. 3, pp. 479 – 491, June 2006.

[13] I. M. Horowitz, *Synthesis of Feedback Systems*. New York: Academic Press, 1963.

[14] A. Papoulis, *Probability, Random Variables, and Stochastic Processes*, 3rd ed. McGraw–Hill, 1991.

[15] *IEEE Standard Specification Format and Test Procedure for Single-Axis Interferometric Fiber Optic Gyros*, The Institute of Electrical and Electronics Engineers Std. 952-1997 (R2008).

[16] P. Welch, "The use of fast fourier transform for the estimation of power spectra: A method based on time averaging over short, modified periodograms," *IEEE Trans. Audio Electroacoust.*, vol. 15, pp. 70 – 73, 1967.